

On-demand heralded MIR single-photon source using a cascaded quantum system

Jake Iles-Smith,^{1,*} Mark Kamper Svendsen,^{2,*} Angel Rubio,^{2,3,4} Martijn Wubs,^{5,6,7} and Nicolas Stenger^{5,6,7}

¹*Department of Physics and Astronomy, The University of Manchester, Oxford Road, Manchester M13 9PL, United Kingdom*

²*Max Planck Institute for the Structure and Dynamics of Matter and Center for Free-Electron Laser Science & Department of Physics, Luruper Chaussee 149, 22761 Hamburg, Germany*

³*Center for Computational Quantum Physics, Flatiron Institute, New York, New York 10010, USA*

⁴*Nano-Bio Spectroscopy Group and European Theoretical Spectroscopy Facility (ETSF), Universidad del País Vasco (UPV/EHU), Av. Tolosa 72, 20018 San Sebastian, Spain*

⁵*Department of electrical and photonics engineering, Technical University of Denmark, 2800 Kgs. Lyngby, Denmark*

⁶*Center for Nanostructured Graphene, Technical University of Denmark, 2800 Kgs. Lyngby, Denmark*

⁷*NanoPhoton – Center for Nanophotonics, Technical University of Denmark, 2800 Kgs. Lyngby, Denmark*

(Dated: May 22, 2024)

We propose a novel mechanism for generating single photons in the mid-Infrared (MIR) using a solid-state or molecular quantum emitter. The scheme utilises cavity QED effects to selectively enhance a Frank-Condon transition, deterministically preparing a single Fock state of a polar phonon mode. By coupling the phonon mode to an antenna, the resulting excitation is then radiated to the far field as a single photon with a frequency matching the phonon mode. By combining macroscopic QED calculations with methods from open quantum system theory, we show that optimal parameters to generate these MIR photons occur for modest light-matter coupling strengths, which are achievable with state-of-the-art technologies. Combined, the cascaded system we propose provides a new quasi-deterministic source of heralded single photons in a regime of the electromagnetic spectrum where this previously was not possible.

I. INTRODUCTION

Single photons lie at the heart of many applications in quantum science and technology. Among these applications, quantum metrology and precision spectroscopy stand out as particularly promising, since they can in principle reach the so-called quantum limit of precision in transmission and absorption spectroscopy [1–4]. This approach holds particular promise in the context of spectroscopy of biological systems [5–8], where stringent power limitations are imposed on conventional spectroscopic techniques to prevent damage of biological samples.

Importantly, the range of degrees of freedom that can be explored through single-photon spectroscopy is intricately tied to the frequency of the generated photons. Specifically, single photons in the visible spectrum are instrumental in investigating electronic processes, whereas photons in the mid- and far-infrared (IR) ranges are indispensable for probing vibrational transitions. Novel quantum light sources in the MIR could enable precise measurements *in vivo* on the single molecular vibration level, understand the fundamental role played by vibrations in quantum matter [9], as well as give us the spectroscopic means to follow chemical reactions in solvents [10, 11]. While there have been significant developments in pushing single-photon sources to the near IR and telecommunication C-bands [12, 13], these quantum

emitters (QEs) rely on well defined electronic transitions, and thus are not able to access the spectral regimes relevant to vibrational transitions. There are, so far, no known materials with band gaps in the MIR able to efficiently produce single photons with high brightness.

In this work, we propose a novel scheme for generating single photons in the mid-infrared (MIR) using a quantum emitter interacting with polar phonon modes, an optical cavity, and a MIR antenna. The protocol consists of a two-part cascaded processes which is shown schematically in Fig. 1: In the first stage, a single Fock state ($|1\rangle$) is prepared in the polar phonon mode through the selective Purcell enhancement of the first phonon sideband. As shown schematically in Fig. 1(i), the successful preparation of the single phonon state is heralded by the emission of an optical photon. The preparation and manipulation of such quantum vibrational states is of significant interest to applications in quantum optomechanics and transduction. However, existing proposals are inherently probabilistic [14–16] and demand advanced time-resolved spectroscopic schemes [17]. In contrast, our protocol can be implemented deterministically with standard photonic/plasmonic cavities if the sideband corresponding to the relevant phonon mode can be spectrally isolated, and crucially is heralded by the emission of a photon via the cavity mode.

In the second stage of our protocol, the excitation in the phonon mode is radiated as a photon by coupling the phonon mode to a resonant antenna structure [18–20], as shown in Fig. 1(ii). By starting with a macroscopic QED description of the quantum emitter and phonon environment, we show that the macroscopic dipole moment of

* These two authors contributed equally

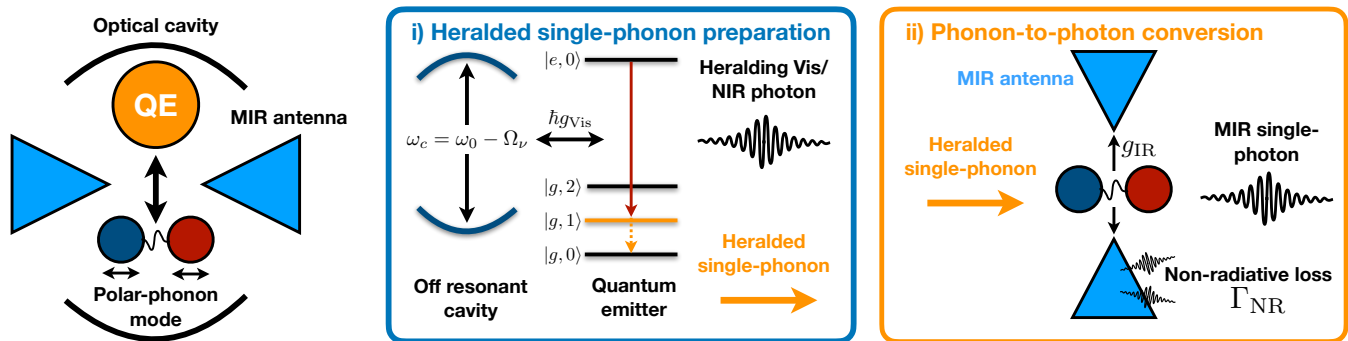


FIG. 1. **A schematic of the MIR-photon generation protocol.** (Left) shows the schematic of a quantum emitter coupled to an optical cavity, interacting with a polar phonon mode. The phonon mode subsequently interacts with a plasmonic or dielectric antenna tuned to the resonance of the phonon mode. The middle and right panels show the two-step photon generation protocol: (i) an initially excited quantum emitter emits a photon in the visible via the first phonon sideband, which is Purcell enhanced through the cavity interaction. The emitted photon is used to herald the generation of a single phonon. (ii) The phonon then radiates as a single MIR photon through the interaction with the MIR antenna structure.

the polar phonon mode enables efficient transfer of excitation to the antenna structure, which is subsequently radiated as a single photon with the same frequency as the phonon mode. Such antennas can be constructed from plasmonic nanostructures [21] in both the visible and IR [22], and allow for the bright emission of single-photons into the far-field [23, 24]. A similar coupling has been proposed by Weatherly *et al* [25] as a means to down-convert classical driving fields from visible to IR frequencies. In contrast to a recent proposal to generate single photons in the MIR [26], our proposed scheme does not depend on a continuous external field driving the emitter in the strong coupling regime, and the emission of the MIR photon is heralded by the presence of a single photon in the visible. Furthermore, our scheme is not restricted to a particular material system, and is applicable to any quantum emitter, solid-state or molecular, coupled to polar phonons.

The manuscript is organised as follows: In section II we derive a Hamiltonian for the emitter-phonon-antenna system that underpins our protocol using macroscopic QED. In section III we characterise the performance of the two-step cascaded system, including generation efficiency and purity of the resulting emitted photon in the MIR. In section IV, we conclude the paper by discussing how the protocol can be realised in material based systems, including defects in two-dimensional (2D) materials, inorganic nanocrystals, and molecular systems.

II. MODEL FOR A CASCADED QUANTUM EMITTER IN THE MID IR

We start by considering a molecular system, with electronic and nuclear degrees of freedom governed by the Hamiltonian H_{mol} . Within the length gauge, the interaction between the molecule and the electromagnetic de-

grees of freedom are given by [27, 28],

$$\hat{H} = \hat{H}_{\text{mol}} + \frac{1}{2} \sum_{\alpha=1}^N \left(\hat{p}_{\alpha}^2 + \omega_{\alpha}^2 \left[\hat{q}_{\alpha} + \frac{\lambda_{\alpha}}{\omega_{\alpha}} \cdot \hat{\boldsymbol{\mu}}_{\text{total}} \right]^2 \right), \quad (1)$$

where ω_{α} , \hat{p}_{α} , \hat{q}_{α} are respectively the frequency, momentum- and displacement operators associated with photon mode α . The total dipole moment can be decomposed into a sum of the nuclear- and electronic dipole moments, $\hat{\boldsymbol{\mu}}_{\text{total}} = \hat{\boldsymbol{\mu}}_{\text{nu}} + \hat{\boldsymbol{\mu}}_{\text{el}}$. The coupling between the molecular degrees of freedom and the electromagnetic field occurs through the matrix elements λ_{α} . These matrix elements can be related to the dyadic Green's function of the electromagnetic environment in a quantitative way and generally reflect the dipole spectral density of the electromagnetic environment [29]. We discuss this relation and its implication for realistic structures in the supplementary information.

As our model of the intra-molecular Hamiltonian, we consider a single polar phonon mode coupled to a two-level molecule, with ground and excited states, $|g\rangle$ and $|e\rangle$ respectively. In the diabatic basis, and assuming linear electron-phonon coupling, the molecular Hamiltonian takes the form [25],

$$\hat{H}_{\text{mol}} = (E_{\text{vert}} - \Omega_{\nu} Q_e^{(0)} \hat{Q}_{\nu}) |e\rangle \langle e| + \frac{1}{2} \left(\hat{P}_{\nu}^2 + \Omega_{\nu}^2 \hat{Q}_{\nu}^2 \right). \quad (2)$$

Here Ω_{ν} is the frequency of the polar phonon mode, \hat{Q}_{ν} (\hat{P}_{ν}) is the phonon configurational coordinate displacement (momentum) operator. $Q_e^{(0)}$ is the configurational coordinate displacement along that phonon mode associated with the minimum of the excited state potential energy surface (PES) relative to that of the ground state. The transition energy associated with the ground and excited state is given by $E_{\text{vert}} = \hbar\omega_{\text{eg}} + S\hbar\Omega_{\nu}$, where $S = (Q_e^{(0)})^2 / (2\hbar\Omega_{\nu})$ is the Huang-Rhys parameter, and $\hbar\omega_{\text{eg}}$ is the energy difference between the minima of

the ground- and excited state PES. We can express the molecular Hamiltonian within second quantisation notation, using $\hat{Q}_\nu = \sqrt{\hbar/2\Omega_\nu}(\hat{b}^\dagger + \hat{b})$, such that

$$H_{\text{mol}} = (E_{\text{vert}} - \hbar\eta_\nu(\hat{b}^\dagger + \hat{b}))|e\rangle\langle e| + \hbar\Omega_\nu\hat{b}^\dagger\hat{b}, \quad (3)$$

where we have defined $\hbar\eta_\nu = Q_e^{(0)}\sqrt{\hbar\Omega_\nu/2}$.

A. Coupling the electron-phonon system to the electromagnetic environment

In order to study the impact of the electromagnetic environment on the coupled electron-nuclear system, we can expand the dipole operator in the diabatic basis. The electronic dipole operator takes the standard form $\hat{\boldsymbol{\mu}}_{\text{el}} = \boldsymbol{\mu}_{eg}\hat{\sigma}_x$, where we have defined the Pauli operator $\hat{\sigma}_x = (|e\rangle\langle g| + \text{h.c.})$ and neglected the permanent dipole contribution. The nuclear dipole moment, up to first order in the phonon displacement and neglecting the permanent dipole moment of the atomic lattice, is, $\hat{\boldsymbol{\mu}}_{\text{nu}}(\hat{Q}_\nu) \approx \boldsymbol{\mu}_{\text{N}}\sqrt{\frac{2\Omega_\nu}{\hbar}}(\hat{Q}_\nu - Q_g^{(0)})$, where $\boldsymbol{\mu}_{\text{N}}$ describes the magnitude of the nuclear dipole moment, and may be related to the Born charges of the system as will be discussed in Sec. IV. The above operator describes the change of the dipole moment due to the displacement along the phonon mode, which leads to infrared activity.

With an expression for the dipole moment operator in hand, we can consider the coupling to the electromagnetic environment which we assume consists of two parts, as shown schematically in Fig. 1: a single-mode optical cavity in the visible range with mode frequency ω_{Vis} , and a MIR antenna with frequency ω_{MIR} . As shown by Katz *et al.* [18], it is often well justified to approximate the antenna structure by a single damped mode. Both single-mode electromagnetic environments are defined by the displacement (momentum) operators \hat{q}_α (\hat{p}_α) with $\alpha = \text{Vis, MIR}$. Using the Hamiltonian Eq. 1, and expanding the dipole moment operator, we have,

$$\begin{aligned} \hat{H} = & \hat{H}_{\text{mol}} + \sum_{\alpha=\text{Vis, IR}} \frac{1}{2} (\hat{p}_\alpha^2 + \omega_\alpha^2 \hat{q}_\alpha^2) + \omega_{\text{Vis}} \boldsymbol{\lambda}_{\text{Vis}} \hat{q}_{\text{Vis}} \hat{\boldsymbol{\mu}}_{\text{el}} \\ & + \omega_{\text{IR}} \boldsymbol{\lambda}_{\text{IR}} \hat{q}_{\text{IR}} \hat{\boldsymbol{\mu}}_{\text{nu}} + \frac{(\boldsymbol{\lambda}_{\text{V}} \cdot \hat{\boldsymbol{\mu}}_{\text{Tot}})^2 + (\boldsymbol{\lambda}_{\text{IR}} \cdot \hat{\boldsymbol{\mu}}_{\text{Tot}})^2}{2}. \end{aligned} \quad (4)$$

Since the optical and MIR transitions are far off-resonance, we have neglected the coupling between the electronic-dipole transition and the MIR antenna, and similarly for the phonon mode and the optical cavity. The final term in Eq. (4) is the dipole self-energy term. In our construction, it will contain three different contributions: the electronic-, the nuclear-, and the cross nuclear-electronic dipole self energies. In general, keeping all these contributions is crucial to ensure the stability of the coupled system and the existence of a ground-state [30]. However, under the two-level approximation that we apply in this work, the electronic contribution is

proportional to $\hat{\sigma}_x^2 = \mathbb{I}_2$ and it thus manifests as a simple energy shift of both the ground and excited states. The electronic contribution can therefore be safely neglected in our setting.

We now move to a second quantised notation, such that $\hat{q}_\alpha = \sqrt{\hbar/2\omega_\alpha}(\hat{a}_\alpha^\dagger + \hat{a}_\alpha)$, yielding the Hamiltonian,

$$\begin{aligned} \hat{H} = & \hat{H}_{\text{mol}} + \sum_{\alpha=\text{V,IR}} \hbar\omega_\alpha \hat{a}_\alpha^\dagger \hat{a}_\alpha \\ & + \hbar g_{\text{Vis}} \hat{\sigma}_x (\hat{a}_{\text{Vis}} + \hat{a}_{\text{Vis}}^\dagger) + \hbar g_{\text{IR}} (\hat{b}^\dagger + \hat{b}) (\hat{a}_{\text{IR}} + \hat{a}_{\text{IR}}^\dagger) \\ & + \hbar \eta_c \hat{\sigma}_x (\hat{b}^\dagger + \hat{b}) + \hbar \delta_c (\hat{b}^\dagger + \hat{b})^2. \end{aligned}$$

Where we have introduced the standard light-matter coupling strengths [29],

$$\hbar g_{\text{Vis}} = \sqrt{\frac{\hbar\omega_{\text{Vis}}}{2}} \boldsymbol{\mu}_{eg} \cdot \boldsymbol{\lambda}_{\text{Vis}}, \quad (5)$$

$$\hbar g_{\text{IR}} = \sqrt{\frac{\hbar\omega_{\text{IR}}}{2}} \boldsymbol{\mu}_{\text{N}} \cdot \boldsymbol{\lambda}_{\text{IR}}. \quad (6)$$

and the counter-term energies,

$$\eta_c = 2 \left(\frac{g_{\text{Vis}}^2 \mu_{\text{N}}}{\omega_{\text{Vis}} \mu_{eg}} + \frac{g_{\text{IR}}^2 \mu_{eg}}{\omega_{\text{IR}} \mu_{\text{N}}} \right), \quad (7)$$

$$\delta_c = \frac{g_{\text{IR}}^2}{\omega_{\text{IR}}} + \frac{g_{\text{Vis}}^2}{\Omega_{\text{Vis}}} \left(\frac{\mu_{\text{N}}}{\mu_{eg}} \right)^2, \quad (8)$$

where we have introduced $\mu_\alpha = |\boldsymbol{\mu}_\alpha|$. Note that the counter term stemming from the electron-nuclear dipole self energy contribution, the term proportional to $\hat{\sigma}_x(\hat{b}^\dagger + \hat{b})$, will be heavily suppressed since the phonon mode and optical transition are far detuned from one another. We therefore neglect this term. Furthermore, we assume that the remaining counter term is dominated by its first term, such that $\delta_c \approx g_{\text{IR}}^2/\omega_{\text{IR}}$.

Finally, since the frequency associated to the optical transition is much larger than any other energy scale, we can make the rotating wave approximation, placing the visible cavity coupling in Jaynes-Cummings form,

$$\begin{aligned} \hat{H} \approx & \hat{H}_{\text{mol}} + \sum_{\alpha=\text{V,IR}} \hbar\omega_\alpha \hat{a}_\alpha^\dagger \hat{a}_\alpha + \hbar g_{\text{Vis}} (\hat{\sigma}^\dagger \hat{a}_{\text{Vis}} + \hat{\sigma} \hat{a}_{\text{Vis}}^\dagger) \\ & + \hbar g_{\text{IR}} (\hat{b}^\dagger + \hat{b}) (\hat{a}_{\text{IR}} + \hat{a}_{\text{IR}}^\dagger) + \hbar\Omega_\nu \hat{b}^\dagger \hat{b} + \hbar\delta_c (\hat{b}^\dagger + \hat{b})^2. \end{aligned} \quad (9)$$

B. Master equation for the cascaded MIR source

Now that we have a Hamiltonian for the coupled system, we wish to consider its dynamics. We will do this through the master equation formalism, allowing us to account for finite lifetime of the cavity, antenna, and phonon modes, which are assumed to have spectral widths κ_{Vis} , κ_{IR} , and γ respectively. Here $\kappa_{\text{IR}} = \Gamma_{\text{R}} + \Gamma_{\text{NR}}$ contains both a radiative contribution Γ_{R} to the far field, and a non radiative contribution Γ_{NR} related to internal losses of the antenna (see discussion in

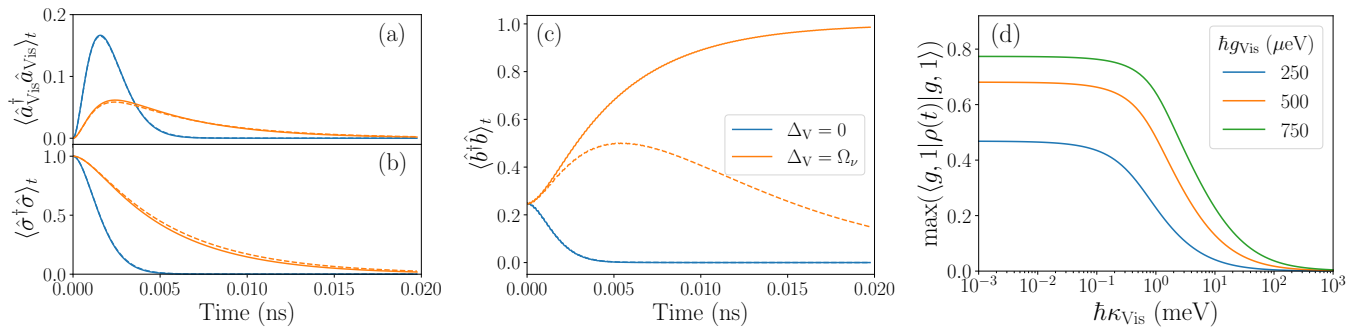


FIG. 2. **Dynamical preparation of a single phonon state:** (a) and (c) show the cavity occupation and emitter dynamics respectively for a cavity tuned to the ZPL (blue) and first sideband transition (orange) resonant. The dashed curves show the effect of including intrinsic losses of the phonon mode. Parameters used here are $\hbar g_{\text{vis}} = 500 \mu\text{eV}$, $\hbar \kappa_{\text{vis}} = 1.5 \text{ meV}$, $\hbar \Omega_{\nu} = 180 \text{ meV}$, and $\hbar \eta_{\nu} = 90 \text{ meV}$. The intrinsic losses of the phonon mode is either $\hbar \gamma = 0$ (solid curves) or $\hbar \gamma = 0.1 \text{ meV}$. (c) The phonon occupation for the ZPL and first sideband enhanced emission with (dashed) and without (solid) intrinsic losses in the phonon mode. (d) The maximum transient population of the first Fock state in the ground state manifold. The intrinsic loss parameter of the phonon mode is set to $\hbar \gamma = 0.1 \text{ meV}$.

section IIIB). Assuming all phonon and photon modes have Lorentzian profiles, then we may write the master equation as,

$$\begin{aligned} \frac{\partial \rho(t)}{\partial t} = & -\frac{i}{\hbar} [\hat{H}, \rho(t)] + \frac{\kappa_{\text{vis}}}{2} \mathcal{L}_{\hat{a}_{\text{vis}}}[\rho(t)] \\ & + \frac{\kappa_{\text{IR}}}{2} \mathcal{L}_{\hat{a}_{\text{IR}}}[\rho(t)] + \frac{\gamma}{2} \mathcal{L}_{\hat{b}}[\rho(t)] \end{aligned} \quad (10)$$

where $\rho(t)$ is the reduced density operator of the electronic-cavity-antenna-phonon system. We have also introduced the Lindblad dissipator $\mathcal{L}_{\hat{O}}[\rho] = 2\hat{O}\rho\hat{O}^\dagger - \hat{O}^\dagger\hat{O}\rho - \rho\hat{O}^\dagger\hat{O}$. We can solve this master equation numerically to extract the optical properties of the composite system in both the IR and visible spectral regime.

III. CASCADED QUANTUM SYSTEM FOR MIR PHOTON EMISSION

As shown schematically in Fig. 1, to generate a single photon in the MIR, we first need to generate an optical photon, which deterministically prepares a single phonon state, before converting this phonon state into a MIR photon. In this section, we shall first consider each step in the process independently in order to illustrate the mechanisms involved, before combining them as a single cascaded process.

A. Single phonon generation

We start by considering the process by which a single phonon state is deterministically prepared. In order to illustrate this, we initially consider a phonon mode in the absence of the MIR antenna and intrinsic losses (i.e. $g_{\text{IR}} = \gamma = 0$). We consider the quantum emitter to be initially prepared in its excited state, with the phonon

mode prepared in the ground state of the PES associated with the excited electronic configuration, i.e., the coherent state $|S = \eta_{\nu}/\Omega_{\nu}\rangle$, and with the cavity in the vacuum state.

Upon emitting a photon through the cavity, the resulting state of the phonon mode will be dependent on the cavity parameters. In the absence of the cavity, the emission behaviour is governed by the Frank-Condon principle, in which each transition is weighted by the overlap between phonon states associated to the ground and excited state PES, that is $\chi_n = |\langle S|n\rangle|^2$, where $|n\rangle$ are the Fock states associated to the electronic ground state configuration.

However, an optical cavity can suppress or enhance optical transitions depending on the cavity parameters. For example, a cavity resonant with the ZPL ($\Delta_{\nu} = 0$) will enhance emission through the ZPL while suppressing phonon sideband processes. This is an effect commonly used by the on-demand single photon source community to enhance an emitter's indistinguishability and efficiency [31–33]. The blue curves in Fig. 2(a-c) show the dynamics for the optical cavity, emitter, and phonon mode respectively with a cavity that is on resonance with the zero-phonon line in the bad-cavity limit. Here we see a Purcell enhanced exponential decay from the emitter, where excitation is transferred to the cavity mode. If we consider the phonon occupation in Fig. 2(c), we see from an initial phonon occupation given by the displacement of the initial coherent state, $\langle \hat{b}^\dagger \hat{b} \rangle_{t=0} = (\eta_{\nu}/\Omega_{\nu})^2 = 0.25$, the phonon occupation drops to the ground state of the PES associated to the ground electronic configuration. Thus, by enhancing the ZPL transition, we quasi-deterministically prepare a phonon in its ground state $|g, 0\rangle$ in the long-time limit.

Within this protocol, we wish to deterministically generate a single phonon state. We do this by red-detuning the visible cavity to the first phonon sideband transition ($\Delta_{\nu} = -\Omega_{\nu}$), selectively enhancing the $|e, S\rangle \rightarrow |g, 1\rangle$

transition as shown schematically in Fig. 1(i), while suppressing other emission channels. As shown in Fig. 2(a-b) by the orange curves, this results in a lower Purcell enhancement than the resonant cavity, as the dipole transition rate is reduced by the Frank-Condon factor χ_1 . In contrast to the $\Delta_V = 0$, the phonon population increases as a function of time, trending to unity in the long-time limit, indicating that the $|g, 1\rangle$ state is populated.

When intrinsic loss processes are included for the phonon mode, i.e., $\gamma \neq 0$, the phonon population now has a finite lifetime, and thus decays to the ground-state in the long-time limit, as shown by the dashed curve in Fig. 2(c). However, there remains a significant increase in phonon occupation at early times, suggesting that $|g, 1\rangle$ is still prepared. Fig. 2(d) shows the maximum population in the first Fock state in the ground state manifold (i.e. $|g, 1\rangle$) as a function of cavity widths for a range of coupling strengths. We see that the maximum population monotonically increases with both increasing light-matter coupling strength (g_{vis}) and decreasing cavity width (κ_{vis}). It is important to note, however, that while this maximum population is not unity, this is not a true reflection of the efficiency of the preparation scheme. The cavity drives population through the $|g, 1\rangle$ state, while intrinsic losses deplete the phonon occupation; even in regimes where the losses are high, and thus the maximum phonon occupation is low, the population may still move through the $|g, 1\rangle$ state. Therefore, so long as the phonon to MIR photon conversion is faster than the intrinsic losses, then the conversion efficiency may still approach unity. We will discuss this in the following section.

It is important to note that while we have focused on single-phonon state preparation, a similar strategy can be used to prepare multi-phonon Fock-states. By tuning the optical cavity to the N^{th} -phonon sideband, one can prepare the phonon mode to be in the state $|N\rangle$ after photon emission. With the extraction process described in the subsequent section, it is then possible to generate $|N\rangle$ -photon states in the MIR.

B. Converting single phonon states to MIR photons

In the second part of the protocol illustrated in Fig. 1(ii), we examine the efficiency of radiating a single phonon state as a mid-infrared (MIR) photon through its interaction with an MIR antenna, following the mechanism outlined in Sec. II. We start by tuning the MIR antenna to be resonant with phonon mode ($\omega_{\text{IR}} = \Omega_\nu$), and take the emitter and cavity modes to be in their ground states. The phonon mode is then initialised in the single-excitation Fock state $|1\rangle$. Fig. 3(a) shows the phonon mode occupation as a function of time both with (solid) and without (dashed) intrinsic losses γ for several different MIR-cavity parameters. Here we see a relaxation of the phonon population to the ground state, the rate of

which is Purcell enhanced by the MIR-cavity. This behaviour is reflected in the dynamics of the MIR antenna, as shown by Fig. 3(b) where we see population accumulating in the antenna, before decaying exponentially. As expected, the total occupation in the MIR antenna is reduced when intrinsic losses of the phonon mode are incorporated.

It is clear that the occupation of the MIR antenna is sensitive to both the cavity parameters, intrinsic loss of the phonon mode, and the non-radiative loss of the antenna. Therefore, it is necessary to consider the efficiency with which MIR phonons are converted to MIR photons. We do this in analogy to the efficiency defined in cavity QED [33], where the efficiency is given by,

$$\varepsilon = \frac{\Gamma_{\text{R}} \mathcal{P}_{\text{MIR}}}{\gamma \mathcal{P}_{\text{NR}} + (\Gamma_{\text{R}} + \Gamma_{\text{NR}}) \mathcal{P}_{\text{MIR}}}, \quad (11)$$

where we have defined the powers as,

$$\mathcal{P}_{\text{MIR}} = \int_0^\infty \langle a_{\text{IR}}^\dagger a_{\text{IR}} \rangle_t dt \quad \text{and} \quad \mathcal{P}_{\text{NR}} = \int_0^\infty \langle b^\dagger b \rangle_t dt. \quad (12)$$

The efficiency, as defined by Eq. 11 is plotted in Fig. 4 as a function of IR coupling-strength and intrinsic losses of the phonon mode for an idealised MIR antenna with $\Gamma_{\text{NR}} = 0$. Here we see that there is clear competition between intrinsic losses of the phonon mode and the Purcell enhanced emission rate through the MIR antenna determined by the MIR coupling strength $\hbar g_{\text{IR}}$. To ensure efficient conversion of the phonon to MIR, the Purcell enhanced emission rate must exceed the intrinsic losses of the phonon mode. For small values of γ , almost unity efficiency can be achieved with moderate values of the coupling strength g_{IR} . However, as the intrinsic loss of the phonon increases, one needs increasingly strong phonon-antenna couplings to remove the excitation via the MIR antenna. To account for non-radiative losses of the MIR antenna, one can scale the absolute efficiency by the fraction of photons emitted through the radiative path. We refer the reader to the supplementary information for a consideration of the impact of non-radiative antenna losses on the efficiency.

A final consideration for the efficacy of the MIR photon generation is the purity of the resulting photons, i.e. the degree of anti-bunching of the emitted MIR photons. We can determine this by considering the second-order correlation function of the cavity, such that,

$$g^{(2)}(\tau) = N \int_0^\infty \langle a_{\text{IR}}^\dagger(t) a_{\text{IR}}^\dagger(t+\tau) a_{\text{IR}}(t+\tau) a_{\text{IR}}(t) \rangle dt, \quad (13)$$

where $N^{-1} = \mathcal{P}_{\text{MIR}}^2$ is a normalisation constant. The degree of bunching can be calculated from the coincidence counts at zero time delay, that is, $g^{(2)}(\tau = 0)$. This is shown in Fig. 4(a), which shows the MIR photons with

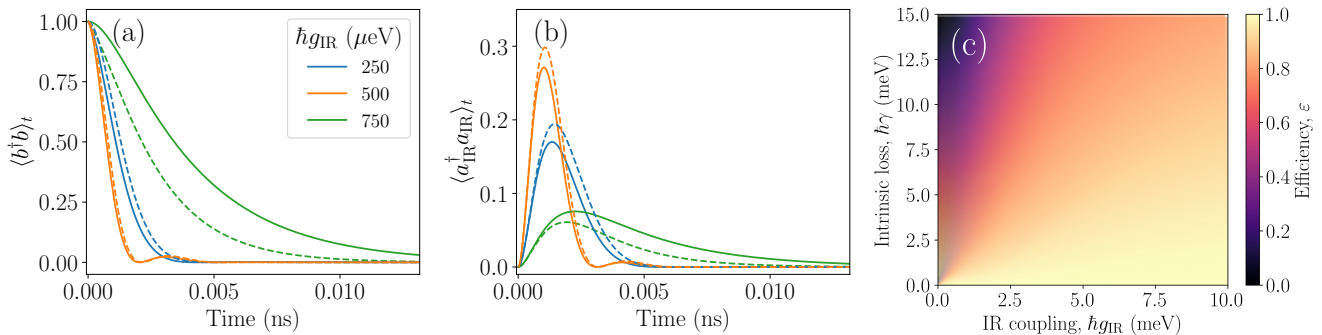


FIG. 3. **The dynamics and efficiency of converting a single phonon into a MIR photon:** (a) The occupation dynamics of the phonon mode when initialised on the $|1\rangle$ state with (dashed) and without (solid) intrinsic losses and an antenna loss rate of $\hbar\kappa_{\text{IR}} = 1.5$ meV. (b) The corresponding population dynamics of the MIR cavity mode. (c) The conversion efficiency of a phonon to a MIR photon as defined by Eq. 11 as a function of the intrinsic loss of the phonon mode γ and coupling strength to the MIR cavity mode g_{IR} . The efficiency was calculated with a loss rate of the MIR cavity of $\kappa_{\text{IR}} = 65$ meV with $\Gamma_{\text{NR}} = 0$. Other parameters are $\hbar g_{\text{Vis}} = 0.5$ meV, $\hbar\kappa_{\text{Vis}} = 0.1$, $\omega_{\text{IR}} = \Omega_{\nu}$, and $\hbar\gamma = 0.1$ meV. All other phonon parameters are the same as in Fig. 2

anti-bunching several orders of magnitude below the classical limit (shown by the dashed red curve) for all parameters chosen. This implies that the photons emitted from the MIR cavity are highly antibunched.

C. Heralded MIR photon generation

Before considering realistic material parameters and systems, we wish to confirm that the MIR photon can be heralded by the emission of a photon from the optical cavity. To do this, we consider the cross correlation function,

$$g_{\text{Her}}^{(2)}(\tau) = N \int_0^{\infty} \langle a_{\text{Vis}}^{\dagger}(t) a_{\text{IR}}^{\dagger}(t+\tau) a_{\text{IR}}(t+\tau) a_{\text{Vis}}(t) \rangle dt \quad (14)$$

where $N^{-1} = \mathcal{P}_{\text{Vis}}\mathcal{P}_{\text{MIR}}$ is a normalisation constant. For the MIR photon to be heralded by the visible photon $g_{\text{Her}}^{(2)}(\tau)$ should be strongly bunched, that is, at zero time delay we expect super-poissonian statistics in the cross-correlation measurements $g_{\text{Her}}^{(2)}(0) > 1$. Fig. 4(b) shows this behaviour for different values of the IR coupling strength g_{IR} , and a fixed intrinsic loss rate of $\hbar\gamma = 1$ meV. Here we see distinct behaviour depending on the value of g_{IR} : for the weakest coupling ($\hbar g_{\text{IR}} = 1$ meV) there is an initial value of bunching, which becomes stronger with increasing τ , suggesting a delay between detecting the heralding photon and the MIR emission. For increasing g_{IR} , and thus Purcell enhancement, this delay is suppressed and the initial bunching increases; this is a consequence of a faster conversion from phonon to MIR photon.

We note in passing that the increase in $g_{\text{Her}}^{(2)}(\tau)$ at later time for weaker coupling could suggest that $\max_{\tau} g_{\text{Her}}^{(2)}(\tau)$ is a more appropriate measure of heralding effi-

ciency. However, here we consider instantaneous heralding ($\tau = 0$) to be the experimentally relevant measure since the heralding and MIR photons should ideally fall within the same detector time bin.

The bunching of the visible and mid-IR photons is also affected by the intrinsic loss of the phonon mode, as shown by Fig. 4(c), where we observe a decrease in the bunching $g_{\text{Her}}^{(2)}(0)$ with increasing γ . This reflects a drop in the MIR photon generation efficiency, which consequently reduces the photon heralding efficiency. However, similar to our efficiency metric, the heralding success rate can be greatly improved by increasing the coupling strength (and thus Purcell enhancement) between the phonon mode and the MIR antenna.

IV. REALISTIC PARAMETERS FOR SOLID-STATE QUANTUM EMITTERS

In this section, we will assess the material parameters of well-known quantum emitters to gauge the experimentally viable coupling strengths between polar phonon modes and an MIR antenna. The interaction between an antenna and a phonon mode is primarily influenced by two factors: the electric field strength generated by the plasmonic or photonic structure and the macroscopic polarization of the material system stemming from the polar phonon mode. Engineering efforts can enhance the electric-field strength through reduction in the mode volume. This can be achieved in nanometre-sized gapped metallic structures, as seen in plasmonic cavities [19, 34, 35], or by computer-aided design in dielectric structures to significantly confine electromagnetic (EM) field modes [36–40]. Furthermore, the polarizability of a phonon mode is intrinsically tied to the chosen material platform.

In the following, we will focus on three distinct plat-

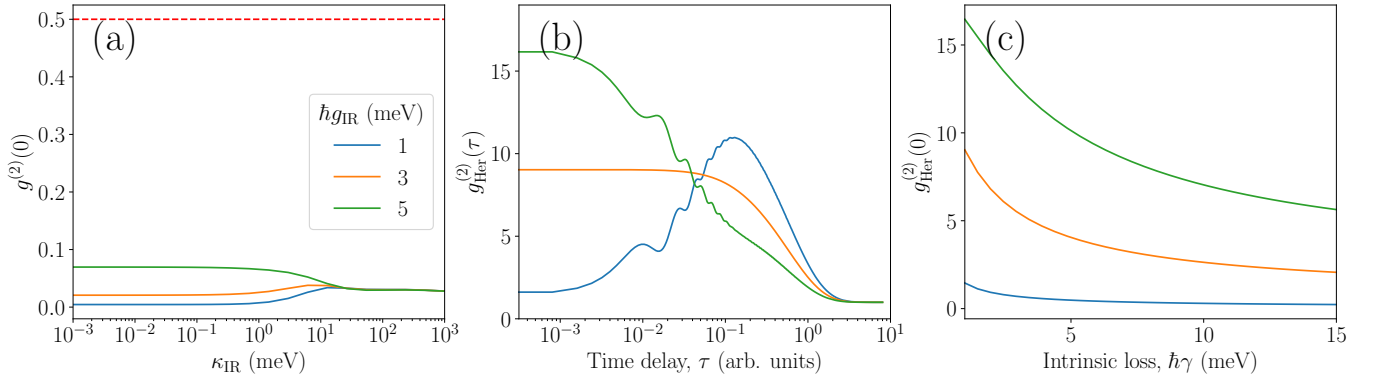


FIG. 4. **Correlations of photons emitted from the MIR cavity:** (a) A graph showing the degree of anti-bunching for the MIR photon emission calculated from Eq. 13 as a function of the MIR cavity losses and for several different values of the MIR coupling given in the legend. The dashed red curve shows the classical limit. (b) The correlations between the heralding photon and the MIR photon emission as a function of time delay with intrinsic loss $\hbar\gamma = 1$ meV, and different values of $\hbar g_{\text{IR}}$ matching those used in (a). (c) Shows the change in the heralding efficiency as a function of intrinsic loss of the phonon mode. All other parameters used match those of Fig. 3

forms for in-depth analysis: color centers in monolayer hexagonal boron nitride (hBN), colloidal quantum dots, and organic molecules. Each platform offers unique properties and challenges in terms of phonon-antenna coupling strength, primarily due to their material-specific polarizability and phonon modes.

A. Estimating the effective dipole moment of a single phonon

For a bulk material, the polarization density induced by the excitation of phonon mode i can be expressed as [41],

$$\Delta \mathbf{P}_i = \frac{1}{\Omega} \sum_{\alpha}^N Z_{\alpha} \boldsymbol{\varepsilon}_{i\alpha}. \quad (15)$$

Here Z_{α} is the Born effective charges of atom α and $\boldsymbol{\varepsilon}_{i\alpha}$ is the displacement of atom α due to the phonon mode i . Ω is the unit cell volume and N is the number of atoms in the unit cell. (In this work, we calculate the Born effective charges using the GPAW and ASE codes [42–44]. Details of these simulations can be found in the Supplementary Information.) Eq. 15 tells us that in order to have an induced polarization by a phonon mode, we need (i) a polar crystal (otherwise $Z_{\alpha} = 0 \forall \alpha$), and (ii) a phonon mode which displaces the atoms such that their overall displacement results in a net movement of charge. In addition to the Born effective charges and the oscillation pattern, the single excitation amplitude is critical to determining the effective dipole moment of a single phonon excitation. In line with our Frank-Condon model of the phonon modes, we will extract the single-phonon displacement amplitude via the well known result for the

quantum harmonic oscillator which states that,

$$\langle n | \hat{x}_{\nu}^2 | n \rangle = (2n + 1) \frac{\hbar}{2\mu_R \omega}, \quad (16)$$

where μ_R is the reduced ion mass of the lattice, ω is the characteristic frequency of oscillator, and $|n\rangle$ is the n^{th} vibrational eigenstate of the harmonic oscillator. Since we are interested in a single phonon mode, we take $n = 1$.

Next we consider the bounds of the effective dipole moment. The lower bound of the induced dipole moment is simply 0 Debye (D). This is because even in a highly polar lattice, some vibrations patterns will result in zero net movement of charge. The upper bound is a more challenging to obtain because it will generally depend both on the material system and on a specific phonon mode.

The paradigmatic polar phonon modes in bulk systems are the longitudinal optical (LO) and transverse optical (TO) phonon modes. These modes are characterized by the anion and cation of the lattice oscillating in opposite directions; along the direction of propagation (LO), and transverse to the direction of propagation (TO). In simple binary crystals, we can thus state that $\boldsymbol{\varepsilon}_{\text{anion}} = -\boldsymbol{\varepsilon}_{\text{cation}}$. We will use these prototypical phonon modes to set the upper bound by assuming that the maximum achievable single-phonon dipole moment is the same as the polarization of a single TO mode excitation in the primitive bulk unit cell. Consequently, the induced polarization within one unit cell by a single TO phonon is,

$$\Omega |\Delta \mathbf{P}| = (|Z_{\text{cation}}| + |Z_{\text{anion}}|) \left(\frac{3\hbar}{2\mu_R \omega} \right)^{1/2}. \quad (17)$$

This therefore leads to the single phonon dipole moment of $|\boldsymbol{\mu}_{\text{N}}| = (|Z_{\text{cation}}| + |Z_{\text{anion}}|) \left(\frac{3\hbar}{2\mu_R \omega} \right)^{1/2}$.

B. Colour centres in hBN

We will first discuss color centers in hBN. hBN is a popular host material for color centers producing single photons in the visible [45–48] which naturally hosts polar phonon modes due to the polar nature of its lattice [49, 50]. For a phonon sideband of interest, one would calculate the Born effective charges and phonon modes of the lattice with the defect included. Eq. 15 would then be used to determine whether the oscillation pattern of the phonon mode responsible for the relevant sideband is such that an overall polarization change occurs. The induced polarization is thus generally both color center and phonon mode specific. Because the number of defect-host material combinations are extremely large, we will refrain from considerations of specific defects in this work and instead use Eq. (17) to estimate the upper limit of the achievable dipole moments. In pristine monolayer hBN, the Boron atoms have a Born effective charge of $Z_B = 2.71e$ for displacements in plane, and the Nitrogen atoms have an effective Born charge of $Z_N = -2.71e$ [51]. For the frequency we will use the LO/TO energy of monolayer hBN of around 170 meV. As shown in Table I, inserting these into Eq. 17 leads to an effective dipole moment of 1.04 D.

C. Colloidal quantum dots

Colloidal quantum dots are another interesting platform for the scheme we envision. In particular, in addition to strong coupling to acoustic sidebands, the emission spectra of InP/ZnSe QDs show clear signs of coupling to the LO/TO mode of the InP crystal in the form of a sideband around 45 meV from the ZPL [52, 53]. When calculating the Born effective charges, these come out to 2.6e and -2.6e for In and P respectively. Performing the same analysis as for h-BN, we thus arrive at an effective dipole moment of 1.05 D. Here it is important to note that unlike the color centers, the QDs actually contain bulk InP. It is therefore reasonable to expect this estimate for bulk InP to be a good measure of what one would measure with a real QD.

Giant shell CdS/Cd colloidal quantum dots display interesting quantum optical properties [54, 55]. These materials host also optical phonon modes featuring high

Material platform	Effective dipole moment
Bulk InP estimate (LO/TO)	1.05 D
Bulk h-BN estimate (LO/TO)	1.04 D
Bulk CdS estimate (LO/TO)	0.9 D
Benzene (Pyrene freq. Ref. [25])	0.11 D

TABLE I. **Comparing material platforms based on the bulk TO mode frequencies:** Effective dipole moment for a single phonon excitation in different material platforms with bulk TO phonon frequencies and Born effective charges calculated using Density Functional Theory.

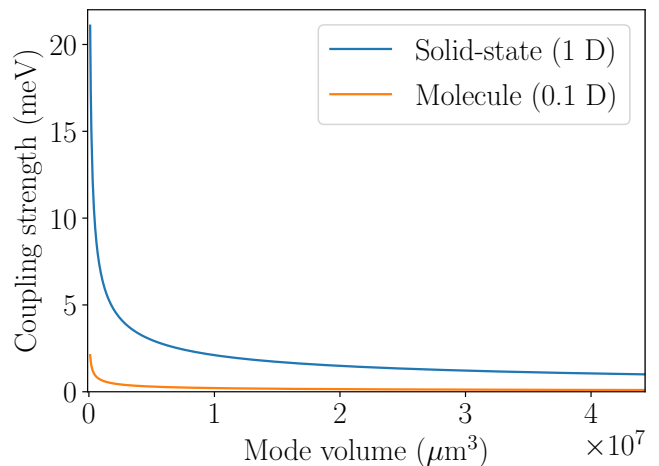


FIG. 5. **Antenna-phonon coupling strength as a function of mode volume:** The expected coupling strength for between a phonon modes with dipole moments characteristic of solid-state (1 D) and molecular (0.1 D) systems. For both systems, we have chosen a material permittivity of $\epsilon = 1.5$ and for a phonon mode with energy $\hbar\omega_{\text{IR}} = 170$ meV.

dipole moments (see Table I). Indeed, strong coupling between optically active (surface) phonon modes in CdS and metallic antenna resonant at THz frequencies has been demonstrated recently [56], thereby also demonstrating the feasibility to couple efficiently nanocrystals with optical antennas at these frequencies. Calculating the Born Effective charges of CdS leads to 2.1e and -2.1e for the Cd and S atoms respectively. Following the same approach as outlined above, we find a dipole moment of 0.9 D. We note that this number is around an order of magnitude lower than the dipole moment of 17 D that one can extract from the experiment in Ref. [56]. This emphasizes that more polar modes than the bulk ones can exist near surfaces (and potentially in defects such as in hBN).

D. Organic molecules

Finally, for comparison, we consider infrared active modes in organic molecules such as methylene blue or PAA where the dipole moment of infrared active mode can range from 0.1D [19] to almost 0.5 D [25], respectively. As a model organic molecule, we calculate the effective charges of the atoms in a benzene molecule. Our calculations show a maximum effective charge of 0.13e and $-0.13e$ for the hydrogen and carbon atoms respectively which is far lower than for the inorganic crystals. Following the same procedure as above for the inorganic crystals, we estimate a dipole moment of 0.11 D as the upper bound for the optically active phonons in benzene. This dipole moment is an order of magnitude lower than for the III-V materials and hBN.

E. Extracting antenna-phonon coupling strength

Given the dipole moment of a material system, we can estimate the expected antenna-phonon coupling strength using Eq. 6, which assuming the dipole moment of the phonon is parallel to the field, we obtain $\hbar g_{\text{IR}} = \sqrt{\hbar \omega_{\text{IR}}/2} |\boldsymbol{\mu}_{\text{N}}| |\boldsymbol{\lambda}_{\text{IR}}|$. This coupling strength will be dependent on the mode volume, V_m , of the antenna structure through the equation $|\boldsymbol{\lambda}_{\text{N}}| \approx 1/\sqrt{\varepsilon \varepsilon_0 V_m}$, where ε_0 (ε) is the vacuum (material) permittivity and V_m is the mode volume. Fig. 5 shows the coupling strength as a function of mode volume for phonon dipole moments characteristic of solid-state and molecular systems. Here we see that for small mode volumes we can obtain coupling strengths necessary for efficient conversion from phonon to MIR photon; these mode volumes are achievable with state-of-the-art plasmonic devices [57, 58] and could soon be reached experimentally with dielectric nanocavities [59].

Our analysis here suggests that III-V materials as well as highly polar 2D materials such as hBN are promising platforms for the transduction process proposed in this work.

V. CONCLUSION

In this work we have demonstrated a unique mechanism to efficiently and quasi-deterministically generate heralded single photons at mid-infrared and even THz frequencies. Importantly, the parameters required for our protocol, including optical transition energies, photonic cavities, optical phonon modes, and MIR antenna coupling strengths, are all realistic and achievable with state-of-the-art materials and nanofabrication. For example, coupling amplitudes between optical tran-

sitions in QE and nanocavities can reach the tens of meV regime [60, 61], and coupling strength between optical phonon modes and MIR-THz antennas of several meV have been demonstrated experimentally [56]. Double antennas devices featuring resonances at visible and MIR frequencies have been proposed theoretically [20] and demonstrated experimentally [35, 62]. Such a design would allow emission rate enhancement of the optical transitions at the first PSB while allowing to convert single polar phonons into MIR photons sent to the far-field. We are therefore confident that our scheme is within reach experimentally using existing technologies.

Our scheme is versatile and may be realised with a wide range of material systems. In particular, polar materials such as low-dimensional hBN and 3D bulk III-V materials host optical phonon modes with dipole moments one order of magnitude higher than for organic molecules, thus allowing more efficient coupling to dielectric or metallic antennas. Our scheme can also be applied to the generation of single polaritons propagating at the surface of materials [63–65], as long as the degrees of freedom of the polarization wave couple strongly to localized electrons or excitons in quantum emitters. The strong correlation between the single photon emitted in the visible and in the MIR works as an interface between the MIR-THz and the Visible-NIR regimes, thereby opening the possibility for quasi-deterministic transduction protocols and could be used in new high fidelity quantum measurements [66].

Overall, our proposed design for new heralded quantum emitters at mid-infrared (MIR) and terahertz (THz) frequencies could enable the creation of innovative spectroscopic methods at the single photon and single phonon level. This could significantly enhance our understanding of quantum phenomena in molecular biology and in novel quantum materials where optical phonons play a significant role.

-
- [1] E. Jakeman and J. Rarity, The use of pair production processes to reduce quantum noise in transmission measurements, *Optics Communications* **59**, 219 (1986).
 - [2] G. Adesso, F. Dell’Anno, S. De Siena, F. Illuminati, and L. A. M. Souza, Optimal estimation of losses at the ultimate quantum limit with non-gaussian states, *Phys. Rev. A* **79**, 040305 (2009).
 - [3] R. Whittaker, C. Erven, A. Neville, M. Berry, J. L. O’Brien, H. Cable, and J. C. F. Matthews, Absorption spectroscopy at the ultimate quantum limit from single-photon states, *New Journal of Physics* **19**, 023013 (2017).
 - [4] P.-A. Moreau, J. Sabines-Chesterking, R. Whittaker, S. K. Joshi, P. M. Birchall, A. McMillan, J. G. Rarity, and J. C. F. Matthews, Demonstrating an absolute quantum advantage in direct absorption measurement, *Scientific Reports* **7**, 6256 (2017).
 - [5] M. A. Taylor, J. Janousek, V. Daria, J. Knittel, B. Hage, H.-A. Bachor, and W. P. Bowen, Biological measurement beyond the quantum limit, *Nature Photonics* **7**, 229 (2013).
 - [6] F. Wolfgramm, C. Vitelli, F. A. Beduini, N. Godbout, and M. W. Mitchell, Entanglement-enhanced probing of a delicate material system, *Nature Photonics* **7**, 28 (2013).
 - [7] M. A. Taylor and W. P. Bowen, Quantum metrology and its application in biology, *Physics Reports* **615**, 1 (2016), quantum metrology and its application in biology.
 - [8] N. Samantaray, I. Ruo-Berchera, A. Meda, and M. Genovese, Realization of the first sub-shot-noise wide field microscope, *Light: Science & Applications* **6**, e17005 (2017).
 - [9] D. Basov, R. Averitt, and D. Hsieh, Towards properties on demand in quantum materials, *Nature materials* **16**, 1077 (2017).
 - [10] K. Heyne and O. Kühn, Infrared laser excitation controlled reaction acceleration in the electronic ground state, *Journal of the American Chemical Society* **141**, 11730 (2019).
 - [11] T. Stensitzki, Y. Yang, V. Kozich, A. A. Ahmed, F. Kössl, O. Kühn, and K. Heyne, Acceleration of a

- ground-state reaction by selective femtosecond-infrared-laser-pulse excitation, *Nature Chemistry* **10**, 126 (2018).
- [12] D. A. Vajner *et al.*, On-demand generation of indistinguishable photons in the telecom c-band using quantum dot devices, *ACS Photonics* **11**, 339 (2024), <https://doi.org/10.1021/acsp Photonics.3c00973>.
- [13] C. L. Phillips, A. J. Brash, M. Godsland, N. J. Martin, A. Foster, A. Tomlinson, R. Dost, N. Babazadeh, E. M. Sala, L. Wilson, J. Heffernan, M. S. Skolnick, and A. M. Fox, Purcell-enhanced single photons at telecom wavelengths from a quantum dot in a photonic crystal cavity, *Scientific Reports* **14**, 4450 (2024).
- [14] C. Galland, N. Sangouard, N. Piro, N. Gisin, and T. J. Kippenberg, Heralded single-phonon preparation, storage, and readout in cavity optomechanics, *Physical Review Letters* **112**, 143602 (2014).
- [15] R. Riedinger, S. Hong, R. A. Norte, J. A. Slater, J. Shang, A. G. Krause, V. Anant, M. Aspelmeyer, and S. Gröblacher, Non-classical correlations between single photons and phonons from a mechanical oscillator, *Nature* **530**, 313 (2016).
- [16] S. Hong, R. Riedinger, I. Marinković, A. Wallucks, S. G. Hofer, R. A. Norte, M. Aspelmeyer, and S. Gröblacher, Hanbury Brown and Twiss interferometry of single phonons from an optomechanical resonator, *Science* **358**, 203 (2017).
- [17] S. T. Velez, K. Seibold, N. Kipfer, M. D. Anderson, V. Sudhir, and C. Galland, Preparation and decay of a single quantum of vibration at ambient conditions, *Physical Review X* **9**, 041007 (2019).
- [18] M. A. Kats, N. Yu, P. Genevet, Z. Gaburro, and F. Capasso, Effect of radiation damping on the spectral response of plasmonic components, *Opt. Express* **19**, 21748 (2011).
- [19] R. Chikkaraddy, R. Arul, L. A. Jakob, and J. J. Baumberg, Single-molecule mid-infrared spectroscopy and detection through vibrationally assisted luminescence, *Nature Photonics* **17**, 865 (2023).
- [20] P. Roelli, D. Martin-Cano, T. J. Kippenberg, and C. Galland, Molecular platform for frequency upconversion at the single-photon level, *Physical Review X* **10**, 031057 (2020).
- [21] L. Novotny and N. van Hulst, Antennas for light, *Nature Photonics* **5**, 83 (2011).
- [22] P. Biagioni, J.-S. Huang, and B. Hecht, Nanoantennas for visible and infrared radiation, *Reports on Progress in Physics* **75**, 024402 (2012).
- [23] A. F. Koenderink, Single-photon nanoantennas, *ACS Photonics* **4**, 710 (2017).
- [24] J. T. Hugall, A. Singh, and N. F. van Hulst, Plasmonic cavity coupling, *ACS Photonics* **5**, 43 (2018).
- [25] C. K. Terry Weatherly, J. Provazza, E. A. Weiss, and R. Tempelaar, Theory predicts UV/Vis-to-IR photonic down conversion mediated by excited state vibrational polaritons, *Nature Communications* **14**, 4804 (2023).
- [26] C. Groiseau, A. I. Fernández-Domínguez, D. Martín-Cano, and C. S. Muñoz, Single-photon source over the terahertz regime, *Physical Review X Quantum* **5**, 010312 (2023).
- [27] F. H. Faisal, *Theory of Multiphoton Processes* (Springer Science & Business Media, 1987).
- [28] I. V. Tokatly, Time-dependent density functional theory for many-electron systems interacting with cavity photons, *Physical Review Letters* **110**, 233001 (2013).
- [29] M. K. Svendsen, K. S. Thygesen, A. Rubio, and J. Flick, Ab initio calculations of quantum light-matter interactions in general electromagnetic environments, *Journal of Chemical Theory and Computation* (2024).
- [30] C. Schäfer, M. Ruggenthaler, V. Rokaj, and A. Rubio, Relevance of the quadratic diamagnetic and self-polarization terms in cavity quantum electrodynamics, *ACS Photonics* **7**, 975 (2020).
- [31] N. Somaschi, V. Giesz, L. De Santis, J. C. Loredó, M. P. Almeida, G. Hornecker, S. L. Portalupi, T. Grange, C. Antón, J. Demory, C. Gómez, I. Sagnes, N. D. Lanzillotti-Kimura, A. Lemaître, A. Auffèves, A. G. White, L. Lanco, and P. Senellart, Near-optimal single-photon sources in the solid state, *Nature Photonics* **10**, 340 (2016).
- [32] T. Grange, N. Somaschi, C. Antón, L. De Santis, G. Coppola, V. Giesz, A. Lemaître, I. Sagnes, A. Auffèves, and P. Senellart, Reducing phonon-induced decoherence in solid-state single-photon sources with cavity quantum electrodynamics, *Phys. Rev. Lett.* **118**, 253602 (2017).
- [33] J. Iles-Smith, D. P. S. McCutcheon, A. Nazir, and J. Mørk, Phonon scattering inhibits simultaneous near-unity efficiency and indistinguishability in semiconductor single-photon sources, *Nature Photonics* **11**, 521 (2017).
- [34] J. J. Baumberg, J. Aizpurua, M. H. Mikkelsen, and D. R. Smith, Extreme nanophotonics from ultrathin metallic gaps, *Nature Materials* **18**, 668 (2019).
- [35] A. Xomalis, X. Zheng, R. Chikkaraddy, Z. Koczor-Benda, E. Miele, E. Rosta, G. A. Vandenbosch, A. Martínez, and J. J. Baumberg, Detecting mid-infrared light by molecular frequency upconversion in dual-wavelength nanoantennas, *Science* **374**, 1268 (2021).
- [36] M. Albrechtsen, B. Vosoughi Lahijani, R. E. Christiansen, V. T. H. Nguyen, L. N. Casses, S. E. Hansen, N. Stenger, O. Sigmund, H. Jansen, J. Mørk, *et al.*, Nanometer-scale photon confinement in topology-optimized dielectric cavities, *Nature Communications* **13**, 6281 (2022).
- [37] M. Xiong, R. E. Christiansen, F. Schröder, Y. Yu, L. N. Casses, E. Semenova, K. Yvind, N. Stenger, O. Sigmund, and J. Mørk, Experimental realization of deep sub-wavelength confinement of light in a topology-optimized InP nanocavity, *Optical Materials Express* **14**, 397 (2024).
- [38] H. Choi, M. Heuck, and D. Englund, Self-similar nanocavity design with ultrasmall mode volume for single-photon nonlinearities, *Physical Review Letters* **118**, 223605 (2017).
- [39] F. Wang, R. E. Christiansen, Y. Yu, J. Mørk, and O. Sigmund, Maximizing the quality factor to mode volume ratio for ultra-small photonic crystal cavities, *Applied Physics Letters* **113** (2018).
- [40] S. Mignuzzi, S. Vezzoli, S. A. Horsley, W. L. Barnes, S. A. Maier, and R. Sapienza, Nanoscale design of the local density of optical states, *Nano Letters* **19**, 1613 (2019).
- [41] R. Resta and D. Vanderbilt, Theory of polarization: a modern approach, in *Physics of ferroelectrics: a modern perspective* (Springer, 2007) pp. 31–68.
- [42] J. Enkovaara, C. Rostgaard, J. J. Mortensen, J. Chen, M. Dulak, L. Ferrighi, J. Gavnholt, C. Glinsvad, V. Haikola, H. Hansen, *et al.*, Electronic structure calculations with gpaw: a real-space implementation of the projector augmented-wave method, *Journal of physics: Condensed Matter* **22**, 253202 (2010).

- [43] A. H. Larsen, J. J. Mortensen, J. Blomqvist, I. E. Castelli, R. Christensen, M. Dulak, J. Friis, M. N. Groves, B. Hammer, C. Hargus, E. D. Hermes, P. C. Jennings, P. B. Jensen, J. Kermode, J. R. Kitchin, E. L. Kolsbjerg, J. Kubal, K. Kaasbjerg, S. Lysgaard, J. B. Maronsson, T. Maxson, T. Olsen, L. Pastewka, A. Peterson, C. Rostgaard, J. Schiøtz, O. Schütt, M. Strange, K. S. Thygesen, T. Vegge, L. Vilhelmsen, M. Walter, Z. Zeng, and K. W. Jacobsen, The atomic simulation environment—a python library for working with atoms, *Journal of Physics: Condensed Matter* **29**, 273002 (2017).
- [44] J. J. Mortensen, A. H. Larsen, M. Kuisma, A. V. Ivanov, A. Taghizadeh, A. Peterson, A. Haldar, A. O. Dohn, C. Schäfer, E. Ö. Jónsson, *et al.*, GPAW: An open python package for electronic structure calculations, *The Journal of Chemical Physics* **160** (2024).
- [45] T. T. Tran, K. Bray, M. J. Ford, M. Toth, and I. Aharonovich, Quantum emission from hexagonal boron nitride monolayers, *Nature Nanotechnology* **11**, 37 (2016).
- [46] M. Fischer, J. M. Caridad, A. Sajid, S. Ghaderzadeh, M. Ghorbani-Asl, L. Gammelgaard, P. Bøggild, K. S. Thygesen, A. V. Krashennnikov, S. Xiao, *et al.*, Controlled generation of luminescent centers in hexagonal boron nitride by irradiation engineering, *Science Advances* **7**, eabe7138 (2021).
- [47] S. Michaelis de Vasconcellos, D. Wigger, U. Wurstbauer, A. W. Holleitner, R. Bratschitsch, and T. Kuhn, Single-photon emitters in layered Van der Waals materials, *Physica Status Solidi (b)* **259**, 2100566 (2022).
- [48] I. Aharonovich, J.-P. Tetienne, and M. Toth, Quantum emitters in hexagonal boron nitride, *Nano Letters* **22**, 9227 (2022).
- [49] D. Wigger, R. Schmidt, O. Del Pozo-Zamudio, J. A. Preuß, P. Tonndorf, R. Schneider, P. Steeger, J. Kern, Y. Khodaei, J. Sperling, *et al.*, Phonon-assisted emission and absorption of individual color centers in hexagonal boron nitride, *2D Materials* **6**, 035006 (2019).
- [50] M. Fischer, A. Sajid, J. Iles-Smith, A. Hötger, D. I. Mikota, M. K. Svendsen, C. Kastl, S. Canulescu, S. Xiao, M. Wubs, *et al.*, Combining experiments on luminescent centres in hexagonal boron nitride with the polaron model and ab initio methods towards the identification of their microscopic origin, *Nanoscale* **15**, 14215 (2023).
- [51] Note that $\sum_{\alpha} Z_{\alpha} = 0$ as expected.
- [52] A. Brodu, M. V. Ballottin, J. Buhot, E. J. Van Harten, D. Dupont, A. La Porta, P. T. Prins, M. D. Tessier, M. A. Versteegh, V. Zwiller, *et al.*, Exciton fine structure and lattice dynamics in InP/ZnSe core/shell quantum dots, *ACS Photonics* **5**, 3353 (2018).
- [53] A. H. Proppe, D. B. Berkinsky, H. Zhu, T. Šverko, A. E. Kaplan, J. R. Horowitz, T. Kim, H. Chung, S. Jun, and M. G. Bawendi, Highly stable and pure single-photon emission with 250 ps optical coherence times in InP colloidal quantum dots, *Nature Nanotechnology* **18**, 993 (2023).
- [54] Y. Chen, J. Vela, H. Htoon, J. L. Casson, D. J. Werder, D. A. Bussian, V. I. Klimov, and J. A. Hollingsworth, “giant” multishell CdSe nanocrystal quantum dots with suppressed blinking, *Journal of the American Chemical Society* **130**, 5026 (2008).
- [55] S. Morozov, S. Vezzoli, A. Myslovska, A. Di Giacomo, N. A. Mortensen, I. Moreels, and R. Sapienza, Purifying single photon emission from giant shell CdSe/CdS quantum dots at room temperature, *Nanoscale* **15**, 1645 (2023).
- [56] X. Jin, A. Cerea, G. C. Messina, A. Rovere, R. Piccoli, F. De Donato, F. Palazon, A. Perucchi, P. Di Pietro, R. Morandotti, *et al.*, Reshaping the phonon energy landscape of nanocrystals inside a terahertz plasmonic nanocavity, *Nature Communications* **9**, 763 (2018).
- [57] F. Benz, M. K. Schmidt, A. Dreismann, R. Chikkaraddy, Y. Zhang, A. Demetriadou, C. Carnegie, H. Ohadi, B. de Nijs, R. Esteban, J. Aizpurua, and J. J. Baumberg, Single-molecule optomechanics in “picocavities”, *Science* **354**, 726 (2016), <https://www.science.org/doi/pdf/10.1126/science.aah5243>.
- [58] H. Herzig Sheinfux, L. Orsini, M. Jung, I. Torre, M. Cecanti, S. Marconi, R. Maniyara, D. Barcons Ruiz, A. Hötger, R. Bertini, S. Castilla, N. C. H. Hesp, E. Janzen, A. Holleitner, V. Pruneri, J. H. Edgar, G. Shvets, and F. H. L. Koppens, High-quality nanocavities through multimodal confinement of hyperbolic polaritons in hexagonal boron nitride, *Nature Materials* **23**, 499 (2024).
- [59] A. N. Babar, T. A. S. Weis, K. Tsoukalas, S. Kadkhodazadeh, G. Arregui, B. Vosoughi Lahijani, and S. Stobbe, Self-assembled photonic cavities with atomic-scale confinement, *Nature* **624**, 57 (2023).
- [60] K.-D. Park, M. A. May, H. Leng, J. Wang, J. A. Kropp, T. Gougousi, M. Pelton, and M. B. Raschke, Tip-enhanced strong coupling spectroscopy, imaging, and control of a single quantum emitter, *Science Advances* **5**, eaav5931 (2019).
- [61] H. Groß, J. M. Hamm, T. Tufarelli, O. Hess, and B. Hecht, Near-field strong coupling of single quantum dots, *Science Advances* **4**, eaar4906 (2018).
- [62] W. Chen, P. Roelli, H. Hu, S. Verlekar, S. P. Amirtharaj, A. I. Barreda, T. J. Kippenberg, M. Kovylyna, E. Verhagen, A. Martínez, *et al.*, Continuous-wave frequency up-conversion with a molecular optomechanical nanocavity, *Science* **374**, 1264 (2021).
- [63] D. Basov, M. Fogler, and F. García de Abajo, Polaritons in van der Waals materials, *Science* **354**, aag1992 (2016).
- [64] T. Low, A. Chaves, J. D. Caldwell, A. Kumar, N. X. Fang, P. Avouris, T. F. Heinz, F. Guinea, L. Martin-Moreno, and F. Koppens, Polaritons in layered two-dimensional materials, *Nature Materials* **16**, 182 (2017).
- [65] D. N. Basov, A. Asenjo-Garcia, P. J. Schuck, X. Zhu, and A. Rubio, Polariton panorama, *Nanophotonics* **10**, 549 (2020).
- [66] M. Kutas, B. E. Haase, F. Rieinger, J. Hennig, P. Bickert, T. Pfeiffer, M. Bortz, D. Molter, and G. von Freymann, Quantum sensing with extreme light, *Advanced Quantum Technologies* **5**, 2100164 (2022).